AIS ARTIFICIAL INTELLIGENCE STUDIES

# AI-Guided Optimal Trajectory Selection in Stereotactic Brain Biopsy

**Emrullah Şahin**[*a], **Muhammed Fatih TALU** [b]

## ABSTRACT

In this study, a new Stereotactic Brain Biopsy System is introduced that enables the biopsy procedure to be conducted in a single session, in contrast to traditional methods requiring two separate sessions. The proposed system comprises two fully automated stages: imaging and planning. The imaging stage involves acquiring MRI and MRA data, while the planning stage automatically calculates the trajectory with the lowest risk score (Entry-Target axis). The target point is determined as the tumor's center, and candidate entry points are defined within a circle centered on the nearest entry point to the target. The system introduces a unique trajectory risk score calculation methodology, considering both geometric and structural risk factors. Geometric risk is assessed based on trajectory length, skull bone thickness, and alignment with the tumor's primary axis, whereas structural risk concerns the trajectory's proximity to independent brain structures. Consequently, automatic segmentation of these brain structures (e.g., vascular tree, ventricles, and functional areas) is necessary. Several features differentiate the proposed biopsy system from existing ones: incorporation of skull thickness information in trajectory detection, provision of objective software output for subjective evaluations during planning, implementation of an innovative risk score approach, adoption of cutting-edge artificial intelligence architectures, elimination of steps typical in classical biopsy (such as MRI-CT registration, visible anatomical structure detection, and verification), and the capacity to perform the biopsy in a single session. The system is intended to be integrated as an extension into the 3D Slicer software and shared with the scientific community in the future.

[a,*] Dumlupınar University,
Engineering Faculty,
Dept. of Software Engineering
43000 - Kütahya, Türkiye
ORCID: 0000-0002-3390-6285

[b] İnönü University,
Engineering Faculty,
Dept. of Computer Engineering
44000 - Malatya, Türkiye
ORCID: 0000-0003-1166-8404

[*] Corresponding author.
e-mail: emrullah.sahin@dpu.edu.tr

**Keywords:** Brain biopsy, Risk factor, Vascular network, Computer-aided tumor detection

**Anahtar Kelimeler:** Beyin biyopsi, Risk faktörü, Damar ağı, Bilgisayar destekli tümör tespiti

Submitted: 25.05.2025
Revised: 12.06.2025
Accepted: 24.06.2025

doi:10.30855/ais.2025.08.01.01

# Stereotaktik Beyin Biyopsisinde Yapay Zekâ Destekli Optimum Rota Seçimi

## ÖZ

Bu çalışmada, geleneksel yöntemlerin iki ayrı seansta gerçekleştirilmesini gerektirdiği beyin biyopsi işlemini tek bir seansta yapmaya olanak tanıyan yeni bir Stereotaktik Beyin Biyopsi Sistemi tanıtılmaktadır. Önerilen sistem, tamamen otomatik iki aşamadan oluşmaktadır: görüntüleme ve planlama. Görüntüleme aşamasında, manyetik rezonans görüntüleme (MRI) ve manyetik rezonans anjiyografi (MRA) verileri elde edilmektedir. Planlama aşamasında ise, en düşük risk skoruna sahip biyopsi rotası (Giriş-Hedef ekseni) otomatik olarak hesaplanmaktadır. Hedef nokta tümörün merkezi olarak belirlenirken, aday giriş noktaları hedefe en yakın yüzey noktasını merkez alacak şekilde tanımlanan bir daire içinde seçilmektedir. Sistem hem geometrik hem de yapısal risk faktörlerini dikkate alan özgün bir biyopsi rotası risk skoru hesaplama yöntemi sunmaktadır. Geometrik risk; rota uzunluğu, kafatası kemik kalınlığı ve rotanın tümörün ana ekseni ile hizalanması gibi ölçütlere dayanmaktadır. Yapısal risk ise, rotanın bağımsız beyin yapılarıyla (örneğin damar ağı, ventriküller ve fonksiyonel alanlar) olan yakınlığına göre değerlendirilmektedir. Bu nedenle, bu beyin yapılarına ait otomatik segmentasyonun gerçekleştirilmesi gerekmektedir. Önerilen biyopsi sistemini mevcut sistemlerden ayıran çeşitli özellikler bulunmaktadır: rota belirleme sürecine kafatası kalınlığı bilgisinin dâhil edilmesi, planlama sürecindeki öznel değerlendirmelere nesnel yazılım çıktıları sağlanması, yenilikçi bir risk skoru hesaplama yaklaşımının uygulanması, ileri düzey yapay zekâ mimarilerinin benimsenmesi, klasik biyopsi yöntemlerinde yer alan MRI-CT kaydı, anatomik yapıların görünürlük temelli tespiti ve doğrulama gibi adımların ortadan kaldırılması ve işlemin tek bir seansta gerçekleştirilebilmesi. Sistem, gelecekte 3D Slicer yazılımına bir eklenti olarak entegre edilmesi ve bilimsel toplulukla paylaşılması hedeflenmektedir.

**To cite this article**: E. Şahin and M. F. Talu, "AI-Guided Optimal Trajectory Selection in Stereotactic Brain Biopsy," *Artificial Intelligence Studies,* vol.8, no.1, pp. 01-19, 2025. doi:10.30855/ais.2025.08.01.01

## 1. Introduction (Giriş)

Artificial intelligence (AI) has rapidly become an essential component across a wide range of industries, including manufacturing [1], energy [2], textile [3], security [4], communication [5], and transportation [6], [7], through its applications in big data analytics [8], large language models (LLMs) [9], [10], and intelligent data processing systems. Among these diverse applications, the healthcare sector stands out as one of the most significantly transformed by AI-driven innovations [11], [12]. The integration of AI into medical workflows has enabled more accurate diagnostics, individualized treatment planning, and improved efficiency in managing complex clinical procedures [13], [14], [15]. Particularly in medical imaging and image-guided interventions, AI technologies offer powerful tools that support clinicians with data-driven insights and high-precision decision-making. In neurosurgery—where even the smallest deviation can have critical consequences—these advances are redefining traditional practices [11], [16]. A notable application within this context is the diagnosis and treatment planning of brain tumors, where obtaining histopathological data through minimally invasive and safe techniques is vital [17] .

Advances in neuroimaging and neurosurgical technologies have significantly enhanced the diagnosis and management of intracranial pathologies [18], [19]. Among these, brain tumors remain one of the most complex and critical conditions due to their heterogeneous nature, varied locations, and potential impact on vital cognitive and motor functions [17], [20]. Early and accurate identification of tumor characteristics plays a pivotal role in improving treatment outcomes and minimizing neurological deficits [20]. In this context, obtaining reliable histopathological information is essential for differentiating tumor types and formulating targeted therapeutic strategies.

Determining the type of brain tumor is crucial for planning the appropriate treatment stages, such as radiation or chemical therapy. Therefore, it is necessary to obtain a sample of the tumor and examine it pathologically. This procedure, known as biopsy, is typically performed through classical surgery. However, classical surgery poses a significant risk when removing a portion of a tumor located in critical areas of sensitive organs such as the brain. In contrast, Stereotactic Biopsy is preferred due to its low risk of complications and the fact that it does not require general anesthesia or craniotomy [21].

There are numerous ongoing studies in the field of stereotactic brain biopsy. For example, Jung et al. [22], conducted a study in which the post-biopsy complications of 42 patients who underwent stereotactic brain surgery between 2015-2020 were examined to determine the reliability of the biopsy. Similarly, Jaradat et al. [23], investigated the reliability of brain stem biopsy in their study. Cheng et al. [24] studied the complications of biopsies performed in different regions of the brain, such as the sellar, pineal, and brainstem, rather than in a single region. Haj-Hosseini et al. [25] proposed a fiber optic probe to guide stereotactic brain tumor biopsy, and it has been found that the tumorous structure is imaged with high accuracy, particularly when the beam is sent on the foundation axis. Ogiwara et al. [26], presented a new biopsy method capable of removing a larger section of a brain tumor using an excision material. However, all these studies are focused on determining or enhancing the reliability of manual stereotactic brain biopsy.

Zanello et al. [27], conducted a systematic review of 42 studies out of 1,543 scientific studies on automated stereotactic planning. These studies covered various applications, including brain biopsy (3 studies), deep brain stimulation (14 studies), trajectory planning for StereoElectroEncephaloGraphy (SEEG) (22 studies), thermal therapy for epilepsy (2 studies), and external ventricular drainage placement (1 study). SEEG involves identifying brain regions with abnormal function and then placing electrodes in these areas through planning. DepthMap and AlternativeFinder are two software tools commonly used in this field [28]. DepthMap uses projective geometry to transfer 3D data to 2D space and estimates depth in the 2D image, thereby providing measurement and visualization capabilities along the trajectory. AlternativeFinder is used for comparing different trajectories. These software tools aid in suitable trajectory planning for epilepsy patients. Zanello highlighted EpiNav, a clinical decision support software developed by the UCL (UK research group), as the standout among others. EpiNav [19] is a 3D neuronavigation software that assists in locating the brain regions causing epilepsy seizures and placing catheters in the relevant area. It is a tool that can identify abnormal brain areas by detecting the vascular structure and white matter (WM) pathways that connect different areas of the brain.

Zanello also emphasized the need for automated stereotactic planning studies to include a brain tumor biopsy module, stating that this is an open working area in the field and that such studies will be needed in the future. Zanello noted that none of the reviewed studies provided information on the future use of the software produced, and that currently, there is no open-source software available for general use, as the software produced is used locally by working groups [27].

Trope et al. [18] conducted a study to examine the differences between automatic and manual trajectory planning using multimodality data obtained from eight patients (six male and two female) with a clear tumor structure. Four scans, including T1, FLAIR, DTI, and fMRI, were obtained from the patients, and they were overlaid on T1. The target point was manually marked on T1, and the outer surface of the skull, ventricles, and blood vessels (>1mm) were segmented. The manually segmented skull was converted into a mesh, and the ventricles were segmented using the region-growing technique of ITKSnap software. The blood vessels were segmented using a watershed and graph cut-based approach, and the segmentation results were manually corrected by a surgeon. The surfaces of the face, ears, hemisphere, cerebellum, and brainstem were removed, and the remaining surface points in the regions were used as candidate entry points. The DTI and fMRI modalities were utilized to identify the visual, auditory, and motor areas. During the planning phase, three different methods were compared: manual, visual, and automatic. In the manual method, the entry point was manually determined. In the visual method, the segmentation results were overlaid in color, and the surgeon determined the entry point using the colored model. In the automatic approach, the skull mesh was reduced to 1000 points, and a risk score was calculated for each point along the trajectory. A different surgeon selected the optimal entry point from the results of the three methods.

Marcus et al. [29] has developed computer-assisted software called SurgiNav for stereotactic brain biopsy. Using the SurgiNav software, a brain surgeon can examine trajectories that allow for the shortest path to reach the tumor by making a perpendicular entry into the skull surface. The surgeon can also assess the potential for encountering vascular structures along these trajectories. SurgiNav automatically calculates the entry and target points, but the brain segmentation algorithm [30] must complete its work before determining these points. The segmentation process takes approximately an hour for a 3D MRI dataset, which is slow and makes SurgiNav unsuitable for clinical use.

Hu et al. [31] conducted a study comparing frame-based stereotactic biopsy with robot-assisted biopsy using MRI and MRA data as input. The study analyzed 151 patient biopsies, with 47 frame-based and 107 robot-based procedures. In the planning phase of the study, SinoPlan software was used, which can automatically extract 3D vascular structures and generate information on whether the planned trajectory will intersect a vessel or not. However, the entry and target points in SinoPlan are manually entered by the surgeon. The quality of the biopsy was evaluated using metrics such as Target Error Point (TPE) and Entry Error Point (EPE). For example, TPE measures the pixel difference between the center of the manually identified tumor and the center of the largest possible circle that can fit inside the tumor structure.

In response to the clinical demand for more reliable, efficient, and patient-friendly stereotactic brain biopsy procedures, we propose a novel system capable of performing the entire biopsy process within a single session. Unlike conventional approaches that typically require two separate stages—each involving imaging, planning, and surgical intervention—our system integrates fully automated imaging and planning modules, thereby minimizing procedural complexity and potential risks. A central innovation of our method is a trajectory risk score calculation framework that evaluates both geometric factors (trajectory length, skull thickness, alignment with the tumor axis) and structural risks (proximity to critical brain structures such as vessels, ventricles, and functional areas). This dual-dimensional risk modeling enhances both safety and surgical accuracy.

Moreover, the proposed system introduces several distinctive contributions to the field: (1) it utilizes skull thickness as a decision-support parameter during trajectory selection, which is typically overlooked in existing systems; (2) it offers objective, software-generated evaluations to support what are often subjective planning decisions; (3) it leverages advanced artificial intelligence architectures to improve automation and precision; and (4) it eliminates classical but redundant steps such as MRI-CT registration and manual identification of anatomical landmarks. These improvements collectively aim

to streamline the biopsy workflow, reduce dependency on operator expertise, and improve reproducibility. To facilitate adoption by the broader research and clinical communities, the system is designed to be integrated as a plugin into the open-source 3D Slicer platform.

The following sections of this manuscript provide details on the materials and methods used in this study, which are explained in Section 2. Specifically, we describe the classical and proposed stereotactic biopsy systems in detail, including their imaging and planning stages. The experimental results of our study are presented in Section 3, where we compare the performance of the classical and proposed systems based on various metrics. Finally, in Section 4, we conclude our study and discuss the potential implications of our proposed system for the field of stereotactic brain biopsy.

## 2. Material and Methods (Materyal ve Yöntem)

### 2.1. Stereotactic Biopsy (Stereotaktik Biyopsi)

Stereotactic biopsy is performed in two sessions. It is given in Figure 1. The first session involves imaging and planning stages, while the second session includes imaging, overlapping, verification, and surgical intervention stages.

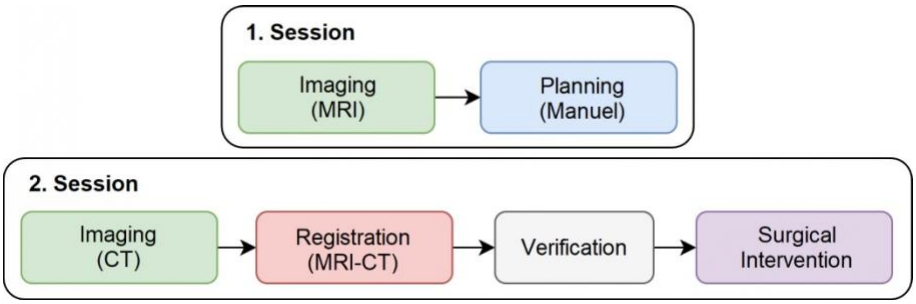


**Figure 1**. The diagram of Two-session Stereotactic Biopsy: Session one includes imaging and planning; session two involves imaging, registration, verification, and surgery.

(İki seanslı Stereotaktik Biyopsi şeması: Birinci seansta görüntüleme ve planlama; ikinci seansta ise görüntüleme, eşleştirme, doğrulama ve cerrahi yer almaktadır.)

#### 2.1.1. Imaging (Görüntüleme)

In this stage, a metal frame is affixed to the patient's head, and an MRI scan is conducted. However, it is possible for the screws used to attach the metal frame to be tightened excessively, resulting in indentations or fractures in the patient's skull bone. As a result, the traditional method of affixing the metal frame can negatively impact patient comfort by requiring the attachment process to be repeated.

#### 2.1.2. Planning (Planlama)

At this stage, all the necessary markings for a stereotactic biopsy are made. This involves determining the entry point from the skull to the center of the tumor (target point) while taking into consideration the tumor location, visible structures such as AC, PC, and MC, brain vessels, and functional regions. Once the optimal entry point is identified, markers are placed in the relevant positions. This stage is time-consuming and typically takes an average of 221 ± 39 minutes (approximately 4 hours), which is why the conventional biopsy approach requires a two-session approach [27].

*Identification of Anatomical Structures*: White oval-shaped fibers, measuring approximately 5 mm in length and oriented vertically, connect the two hemispheres of the brain. The center point of these fibers is known as the AC. The PC is a circular band of white fibers located at the tip of the cerebral aqueduct. The MC is a flattened tissue band that connects both parts of the thalamus. It is roughly 10 mm in diameter and is situated around the middle part of the AC-PC line. The brain surgeon carefully examines the images in three axes (axial, coronal, and sagittal) to identify these structures and typically uses the sagittal axis to place the markers. This process of marking anatomical structures is performed in both sessions, and MRA-CT fusion is conducted using these markers.

*Determining the Target Point*: The target point is located at the center of the tumor mass, which can be detected by analyzing MRI images. Typically, the tumor mass is manually segmented using sagittal axis images, where different colored brushes are used to roughly paint the tumor and non-tumor areas. A circular brush is commonly used, and its size is adjusted according to the size of the tumor. The painted pixels are considered as seeds and provided as input to the "seed expansion" algorithm, which models the pixel values of seeds with the same color value by calculating their mean and covariance matrix. Then, neighboring pixels of seeds are classified based on their similarity to the model (expansion). The model information is updated after each classification, and this process continues until all pixels are classified. However, the expansion algorithm may sometimes lead to misclassification of pixels, which can be corrected by manual interventions using the brush object, resulting in the most accurate segmentation. In the next step, 2D tumor segments from different images are merged to obtain a 3D tumor model, and the center point (target point) of the 3D tumor structure can be easily calculated. An example MRI image demonstrating this process is shown in Figure 2.

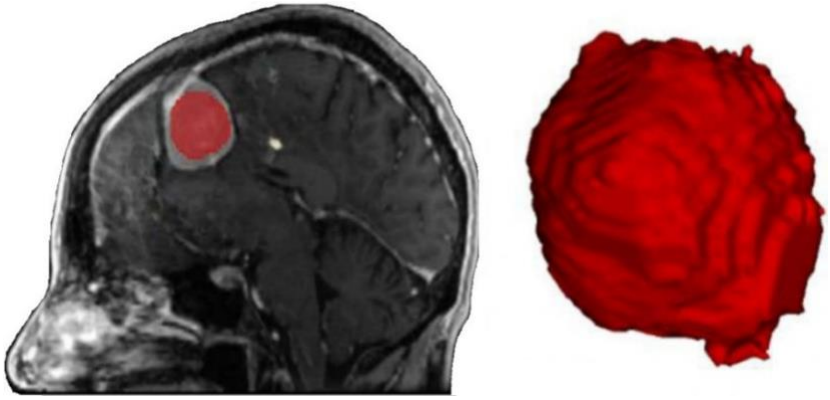

**Figure 2**. Determination of the target point based on tumor center for trajectory planning.
(Rota planlaması için tümör merkezine dayalı hedef noktanın belirlenmesi)

*Determining Entry Point*: This is the most difficult and time-consuming task during the planning phase, as it involves determining the most direct and safest path to reach the target point. To accomplish this, typically 4-5 potential entry points are marked on the 3D skull model, as shown in Figure 3.

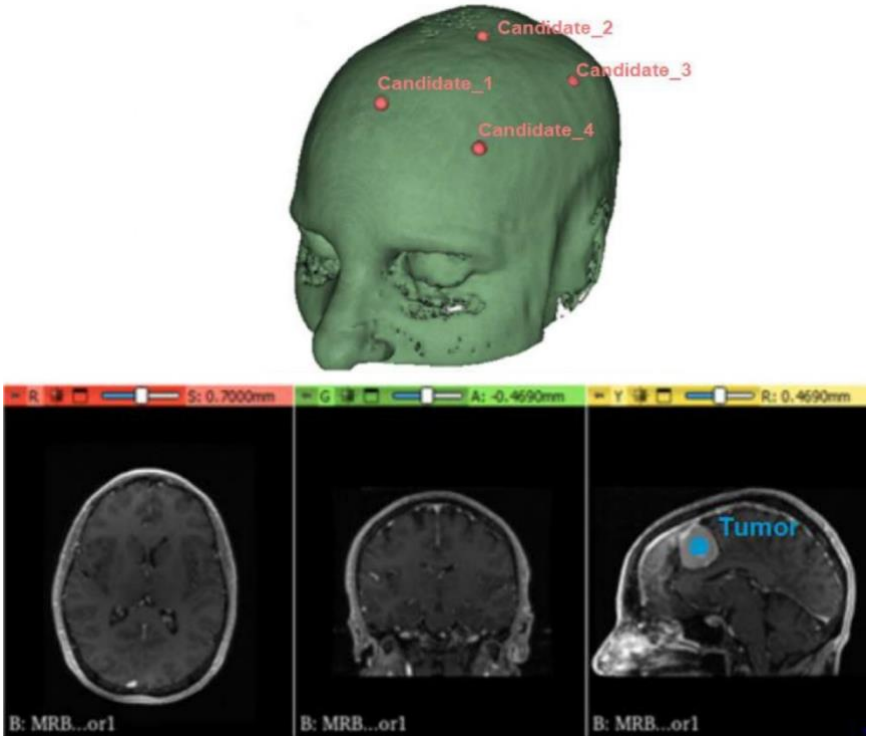


**Figure 3**. Determining candidate entry points around the target for trajectory planning.

(Rota planlaması için hedef çevresindeki aday giriş noktalarının belirlenmesi)

The following steps are performed sequentially for each candidate entry point.

- Measuring the Trajectory Length.
- Checking for Intersection with Vessels on the Trajectory.
- Selection of Entry Point.

*Measuring the Trajectory Length*: To measure the length of the trajectory, a 2D cutting plane is first obtained by passing through the candidate and target points, as shown in Figure 4.

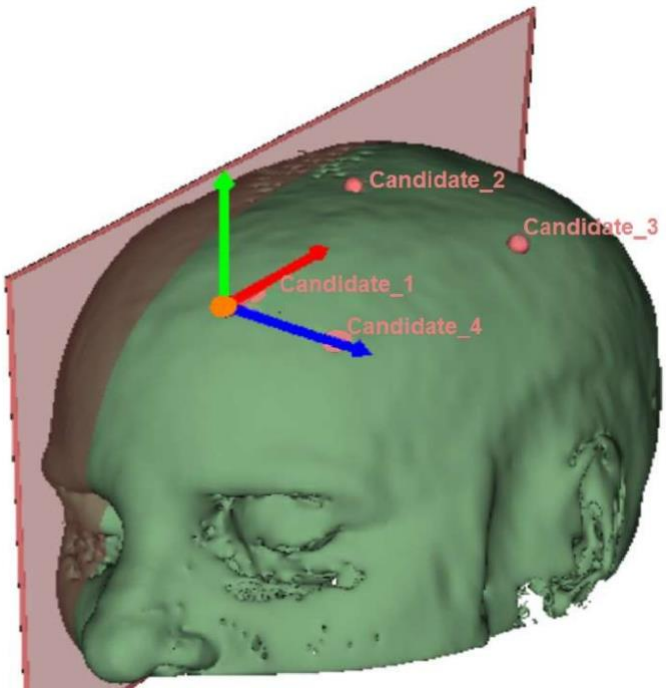


**Figure 4**. Measuring the length of the candidate biopsy trajectory.

(Aday biyopsi rotasının uzunluğunun ölçülmesi)

Once the cutting plane is determined, the 3D skull model is divided into two parts, and either one can be used for measurement. A meter tool is then selected, and the length of the trajectory is measured by selecting the candidate and target points in sequence, as shown in Figure 5.

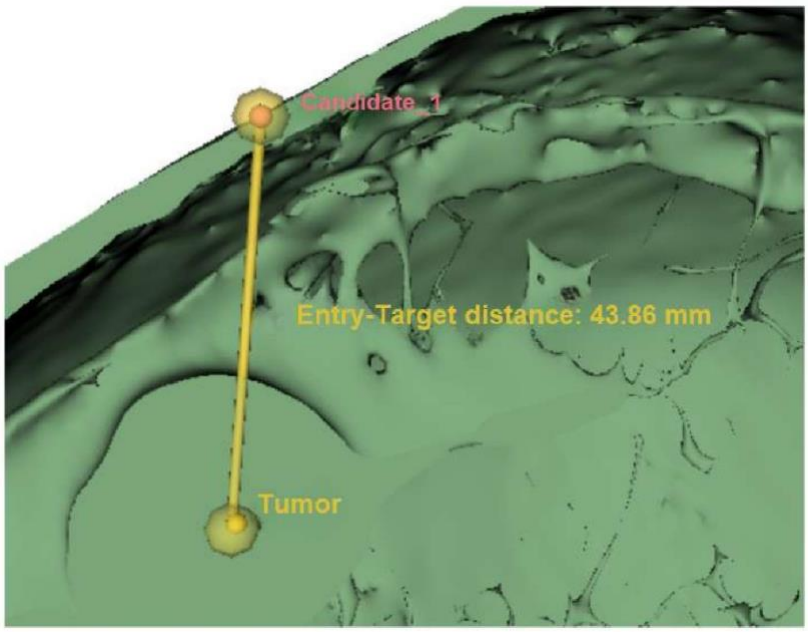


**Figure 5.** Determining the cutting plane and measuring its length using a meter tool.

(Kesme düzleminin belirlenmesi ve uzunluğunun metre aracıyla ölçülmesi)

*Checking for Intersection with Vessels on the Trajectory*: At this stage, it is necessary to verify whether the axis of rotation intersects with the vascular structure, which is done by evaluating the axial, coronal, and sagittal views together. This process is difficult, time-consuming, and carries a high risk of error, as all three images along the axis need to be evaluated simultaneously, as shown in Figure 6. Additionally, in MRI-T1 scans, the vascular structure is not clearly separated from other structures, making it challenging even for experienced surgeons to determine whether the axis of rotation intersects with the vascular structure.

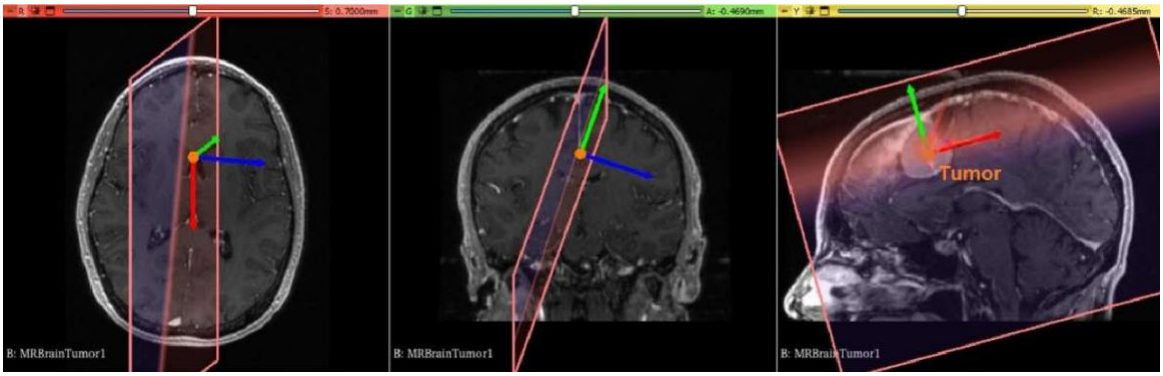


**Figure 6.** Evaluation of the candidate trajectory's overlap with the vascular structure.

(Aday rotanın damar yapısıyla örtüşüp örtüşmediğinin değerlendirilmesi.)

*Selection of Entry Point*: The two processes described above are repeated for each candidate entry point. The results obtained are then evaluated collectively, and the entry point that does not intersect with the vascular structure among the candidate entry points and has the shortest path length is selected as the entry point.

2.1.3. Registration (Eşleştirme)

In the second session, the metal frame is reattached to the patient's head, and a CT scan is conducted. The MRI data obtained in the first session and the CT data obtained in the second session are then aligned using visible anatomical landmarks, as shown in Figure 7.

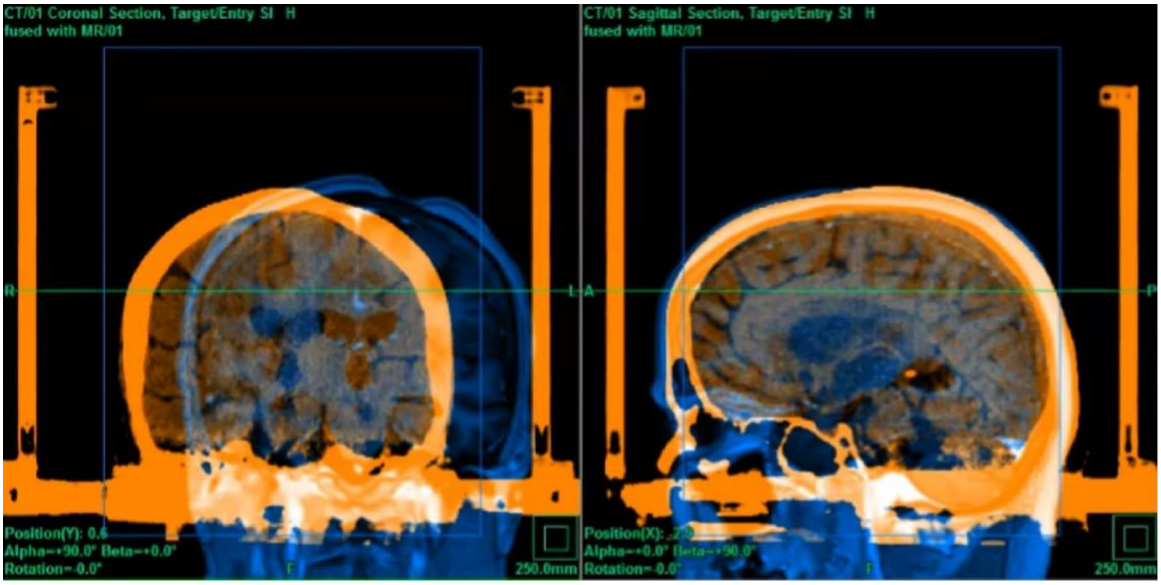


**Figure 7.** The MRI-CT registration process involves aligning (blue) MRI and (orange) CT images.

(MRI-CT eşleştirme süreci, (mavi) MRI ve (turuncu) BT görüntülerinin hizalanmasını içerir)

The registration process involves marking anatomical landmarks on the MRI and CT images and performing a transformation between them. To minimize errors and expedite the process, the surgeon performs a rough manual alignment before running the registration algorithm. 2D MRI and CT image overlay tools are employed to verify the accuracy of the registration. If successful, the entry and target

point coordinates marked on the MRI are transferred to the CT. In case of registration failure, the process is repeated until satisfactory alignment is achieved.

#### 2.1.4. Verification (Doğrulama)

At this stage, the alignment of the biopsy needle to the same point in 3D space before and after registration is verified using a validation tool attached to the patient's head with the metal frame, as shown in Figure 8-left. The angle and distance values on the metal frame are calculated based on the marker information on the MRI image, enabling the determination of the point in 3D physical space corresponding to the tip of the biopsy needle (target point). The position of this point is maintained using the validation tool. Then, the angle and distance values on the metal frame are recalculated based on the CT data, and it is checked whether the tip of the biopsy needle aligns with the same target point. Successful alignment of the validation tool with the biopsy needle tip indicates a successful registration, and the process proceeds to the next stage. If the alignment is unsuccessful, the registration process is repeated until satisfactory alignment is achieved.

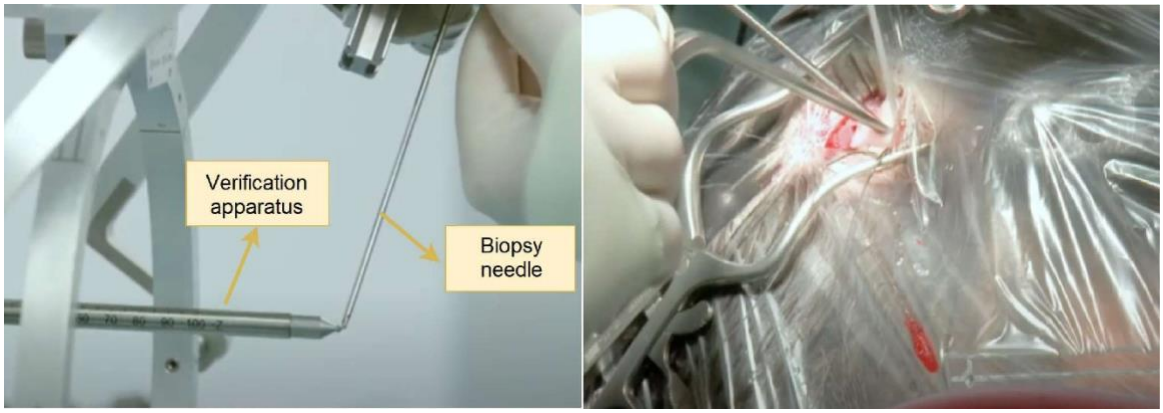


**Figure 8.** Verification and surgical intervention stages of the stereotactic biopsy procedure [32].

(Stereotaktik biyopsi sürecinde doğrulama ve cerrahi müdahale aşamaları)

#### 2.1.5. Surgical Intervention (Cerrahi Müdahale)

At this stage of the procedure, a small incision of 2-3 cm is made on the skull, which is centered around the entry point, as shown in Figure 8-right. It is imperative that the incision is made at an area of the skull where the bone is relatively thin. This allows for ease of cutting by the surgeon and quick healing for the patient. Following the incision, the biopsy needle is carefully inserted from the entry point towards the target point, and a small piece of the tumor is removed for analysis. The needle is then removed, and any necessary stitches are made to close the incision. The patient is then awakened and transferred to the ward for observation. Typically, patients are discharged the day after the procedure and are informed about the results of the biopsy approximately one week later. It is important to note that this procedure carries some risks, such as infection or bleeding, which will be closely monitored by the healthcare team. Nonetheless, with proper care and attention, patients can expect a successful outcome from this procedure.

### 2.2. Proposed Biopsy System (Önerilen Biyopsi Sistemi)

This study introduces a novel automatic stereotactic biopsy system, as shown in Figure 9. This system consists of three main stages: imaging, planning (automatic), and surgical intervention. During the planning stage, the software automatically detects the lowest risk entry-target trajectory, eliminating the need for manual trajectory planning. The system aims to perform the biopsy in a single session, in contrast to the traditional biopsy procedure that requires two sessions. The new system is designed to eliminate dependence on the surgeon and improve patient comfort. Unlike the classical biopsy, the proposed system does not require MRI-CT registration, identification of visible anatomical structures, or verification stages. This results in a faster, more comfortable, and more reliable biopsy for both the patient and the surgeon. In general, the proposed system offers a contemporary biopsy solution that can rival costly systems lacking state-of-the-art artificial intelligence software. It has the potential to revolutionize the biopsy process by providing an automatic and efficient alternative to the traditional

manual approach. While further research and testing are necessary to fully evaluate the efficacy of the new system, the preliminary results are encouraging.

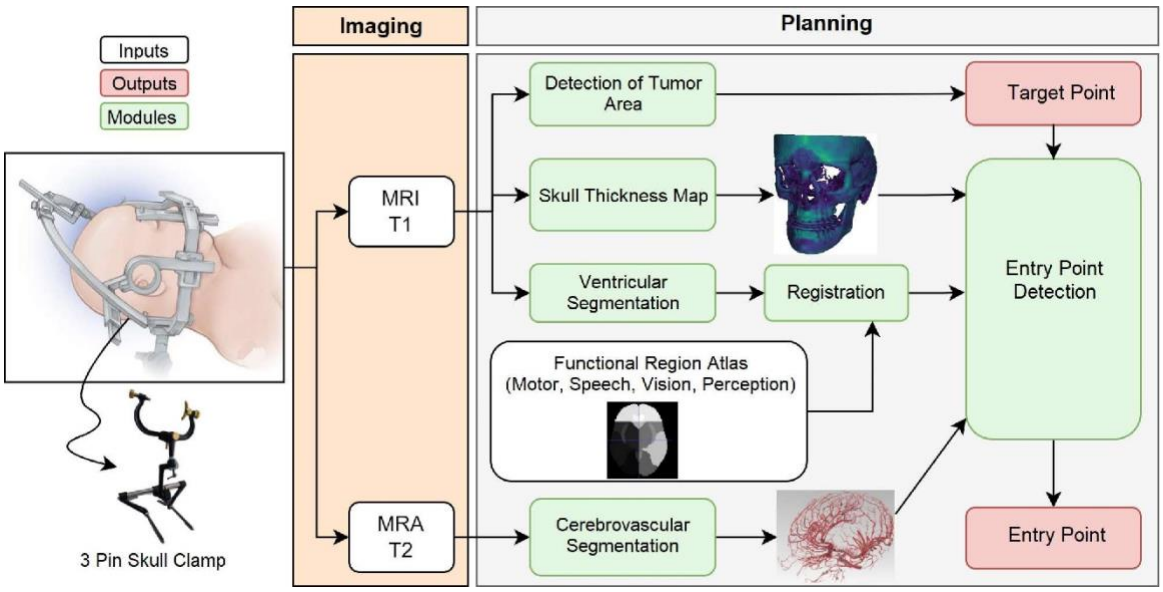


**Figure 9.** Diagram of the Proposed Automatic Modular Brain Biopsy System, illustrating key modules developed to improve safety, speed, and precision in the biopsy process.

(Önerilen Otomatik Modüler Beyin Biyopsi Sisteminin şeması; biyopsi sürecinde güvenlik, hız ve hassasiyeti artırmak üzere geliştirilen temel modülleri göstermektedir.)

2.2.1. Imaging (Görüntüleme)

During this stage, the patient will undergo MRI-T1 and MRA-T2 imaging. The MRA-T2 data will be utilized for segmentation of the vascular network, while the MRI-T1 data will be used for segmentation of other brain structures and calculation of skull thickness. The use of a special frame apparatus is not required during the imaging phase. Instead, a simple 3-pin skull clamp, as shown in Figure 9, can be utilized. This clamp is fixed to the operating table and, if a reference point is established for a robotic system, the proposed system can be utilized in conjunction with a frameless stereotactic biopsy system.

2.2.2. Planning (Planlama)

During the planning phase, automatic processes are performed for tumor, ventricle, cerebrovascular tree, skull thickness, entry point detection, and registration. This stage takes approximately 10 minutes.

*Detection of Tumor Area*: Swin UNETR [33], [34] has been trained on the BraTS 2021 [35] dataset, where it has demonstrated state-of-the-art performance. The BraTS 2021 dataset comprises 1470 3D volumes (1251 for training and 219 for validation) for brain tumor segmentation and is known to contain a sufficient level of color, texture, and shape variations in tumor structures. Swin UNETR leverages shifted windows for self-attention computation in the Swin transformer encoder to extract features at different resolutions [33], [34]. These features are then integrated with each resolution's FCNN-based decoder through skip connections, resulting in accurate brain tumor segmentation.

In this study, we utilized a pre-trained [36] version of the Swin UNETR model that has been trained on the BraTS 2021 dataset and demonstrated high performance. After detecting the tumor structure, we calculated the center point (target point) and basic axis information of the model, with the basic axis information serving as a parameter in determining the entry point.

*Skull Thickness Map*: Talu has previously developed a 3D Slicer extension, which is available on GitHub, that can automatically calculate the thickness map of bone structures in MRI data [37]. Although segmentation of the bone structure from MRI data can be manually performed using 3D Slicer extensions, the developed thickness extension automates the process. This extension comprises two main stages: (1) calculation of the mid-surface plane of the bone structure and (2) calculation of the

distances of bone structure voxels to this plane. Once the segmentation is complete, the thickness extension color-codes skull surface voxels based on their thickness values, and this information is transferred as input to the entry point detection software.

*Ventricular Segmentation*: Ventricles, comprising four adjoining regions, are critical to producing cerebrospinal fluid. Segmentation of these regions has been the focal point of recent studies [38], [39], [40]. Hua et al. [38] implemented a U-Net-like architecture that yielded an accuracy of 85%, whereas Ye et al. [39] utilized MB-Net, achieving a 90% accuracy rate. In our study, we employed the pre-trained version of the state-of-the-art SynthSeg+ model developed by [41], specifically for the task of lateral ventricle segmentation. The SynthSeg+ model fuses structural and anatomical information from MRI scans to segment multiple MR contrasts, resolutions, and orientations. Additionally, it can perform tasks such as cortical parcellation and intracranial volume estimation [41]. The use of this pre-trained model has enabled us to efficiently and accurately segment lateral ventricles, thus significantly facilitating our research process.

*Cerebrovascular Segmentation*: In the realm of cerebral vessel segmentation for automatic brain biopsy systems, diverse models and architectures such as BRAVE-NET [42] and DeepVesselNet [43] have been previously presented in the literature. However, given the absence of pre-trained weights for these models, they pose difficulties in terms of direct application and adaptation. For this reason, we opted to utilize a 3D Residual U-Net [44] architecture for brain vessel segmentation in our automatic brain biopsy system.

The 3D Residual U-Net architecture builds upon the foundational U-Net [45] structure while integrating the principles of residual learning. The traditional U-Net design, known for its proficiency in many medical imaging tasks, is an end-to-end fully convolutional network (FCN) that features a contracting path to capture context and an expansive path for precise localization [44].

The innovation in this 3D Residual U-Net architecture lies in its employment of residual blocks. In residual learning, the model is trained to learn the residual or difference between the input and the desired output, rather than attempting to learn the entire mapping [44]. This is achieved through shortcut connections that bypass one or more layers, allowing for direct backpropagation of the gradient to earlier layers and thereby mitigating the problem of vanishing gradients in deeper networks.

In summary, the 3D Residual U-Net architecture capitalizes on the advantages of the U-Net design and residual learning, offering a potent solution for cerebrovascular segmentation in our automatic brain biopsy system.

*Registration*: Each brain region is responsible for a different functional role and has a different impact on the orbit risk score. For example, surgeons avoid entering the brain region responsible for physical function (motor) during biopsy procedures. Functional regions are determined after obtaining 4D fMRI data. However, the acquisition time for fMRI data is about 30 minutes, and it requires different equipment than a conventional MRI device, which is not widely available. These limitations hinder the use of fMRI in clinical applications. In this study, a different method for detecting functional brain regions is proposed. The proposed method is based on overlapping a common atlas data onto the patient's data. Common atlas data are created by expert surgeons considering the MRI data of many healthy individuals and have widespread use in the field. Atlas data for four different age groups are available from [46]. 27 different brain regions are labeled in each age group's atlas data. In this study, first, which brain region is in which functional region is determined, and 27 brain regions are expressed in 4 different functional regions. Then, the atlas data appropriate for the patient's age overlapped onto the patient's MRI data. During overlapping, segmented ventricular structures are used as reference. That is, the atlas ventricle overlapped onto the patient's ventricle. Thus, functional regions are detected without using fMRI.

*Entry Point Detection*: All points on the surface of the skull are candidate entry points. At this stage, the selection of the entry point with the lowest Entry-Target orbit risk is made. If the $k^{th}$ candidate entry point is denoted by $Cnd_k$ $(Candidate_k)$ and the tumor center is denoted by $t_c$, then $Y_k = [Cnd_k, t_c]$ represents the $k^{th}$ orbit. The risk score of the $Y_k$ orbit is calculated using Equation 1, and the orbit with the lowest risk score among all orbits, $Y_{opt}$, is calculated using Equation 2.

$$risk(Y_k) = \alpha * risk_k^{geo} + (1 - \alpha) * risk_k^{struct} \quad (1)$$

$$Y_{opt} = \min_{k \in CandidateEntries} risk(Y_k) \quad (2)$$

The variable $risk_k^{geo}$ and $risk_k^{struct}$ represent the geometric and structural risks of the $k^{th}$ trajectory, respectively. The parameter $\alpha$ is used to adjust the relative importance of geometric and structural risks. If there are multiple trajectories with the same minimum risk value, the one with the shortest length is preferred.

The geometric risk of the $k^{th}$ trajectory (Equations 3-6) is calculated based on the trajectory length, skull thickness, and similarity to the tumor axis. This risk value is normalized to produce an output in the range of [0-1].

$$risk_k^{geo} = \frac{(length_k + thickness_k + axis_k)}{3} \quad (3)$$

$$length_k = \frac{\|Cnd_k - t_c\| - min(\|Cnd_k - t_c\|)}{max(\|Cnd_k - t_c\|) - min(\|Cnd_k - t_c\|)} \quad (4)$$

$$thickness_k = \frac{Thickness_k - min(Thickness)}{max(Thickness) - min(Thickness)} \quad (5)$$

$$axis_k = cosSimilarity(t_{axis}, Cnd_k - t_c) \quad (6)$$

The structure risk of the $k^{th}$ trajectory is calculated as in Equations 7-11.

$$risk_k^{struct} = vessel_k + ventricle_k + func_k \quad (7)$$

$$vessel_k = c_{vessel} * \sum Dist(BloodVessels) \cap Cylinder_k \quad (8)$$

$$ventricle_k = c_{ventricle} * \sum Dist(Ventricles) \cap Cylinder_k \quad (9)$$

$$func_k = c_{func} * \sum Sulci \cap Cylinder_k \quad (10)$$

$$Sulci = \sum c_m^f * Motor + c_s^f * Speech + c_v^f * Vision + c_p^f * Perception \quad (11)$$

The effects of brain structures on creating risk are different. During surgery, entering a blood vessel is avoided due to its clinical importance and potential for causing hemorrhagic complications. In this study, the structure risk coefficients ($c_{vessel}, c_{ventricle}, c_{func}$) are determined as (0.4,0.3,0.3), respectively. The impact of functional regions (motor, speech, vision, and perception) on the trajectory risk score is determined by coefficients ($c_m^f, c_s^f, c_v^f, c_p^f$) which are determined as (0.4,0.3,0.1,0.2), respectively. These coefficients are quite similar to those used in Trope's study. In Trope's study, the coefficients were determined by five different brain surgery specialists [18].

When calculating structural risk, a rectangular prism (ROI) is used similar to the study by Sparks et al. [47] (Figure 10). The prism, whose width can be adjusted by the surgeon, limits the area where trajectory risk is calculated.

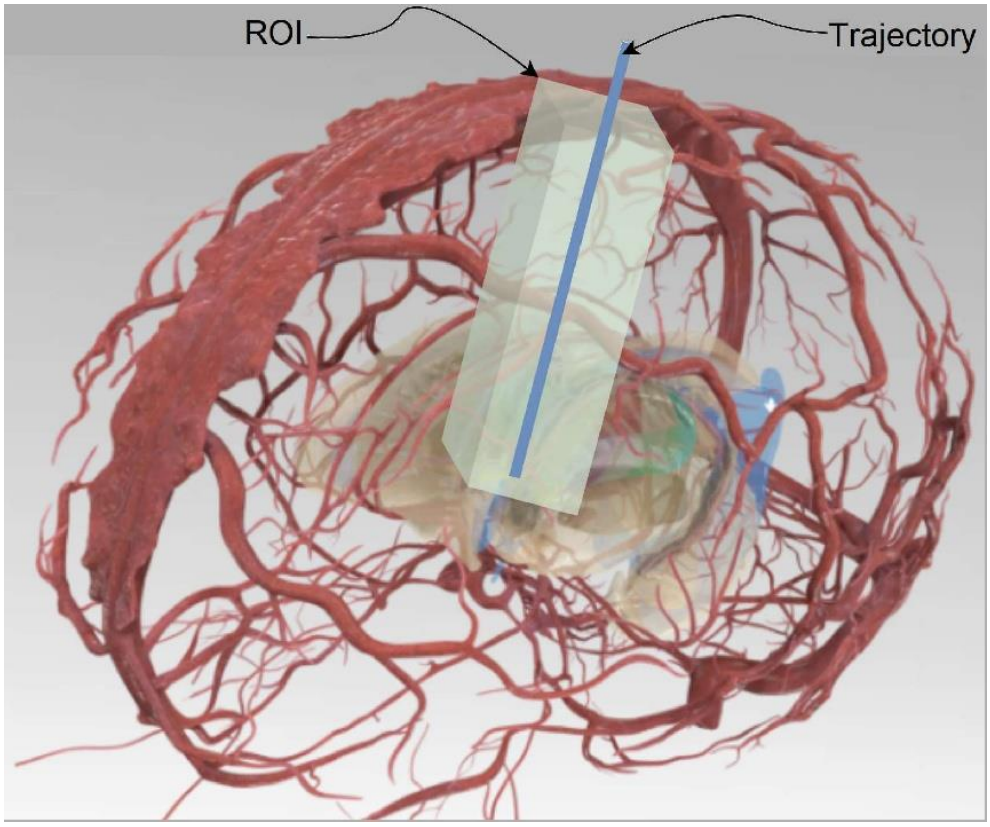


**Figure 10.** The prism (ROI) is used when calculating the risk value of the "Entry-Target" candidate trajectory.

("Giriş-Hedef" aday rotasının risk değeri hesaplanırken prizma (ROI) kullanımı.)

In contrast to Sparks' study, an original risk calculation approach is used in this study. When calculating the trajectory risk score, Sparks evaluates brain structures within the ROI in two levels (Figure 11-left). Thus, he uses only the binary result of whether the trajectory intersects with these structures or not in the risk calculation. In the proposed approach, however, brain structures are evaluated in a grayscale based on their distance from the edge, rather than two-level evaluation (Figure 11-right). This evaluation captures the difference between passing through the center of the structure and passing through the edge. Passing through the center has a higher impact on the risk factor, while passing through the peripheral area has a lower impact.

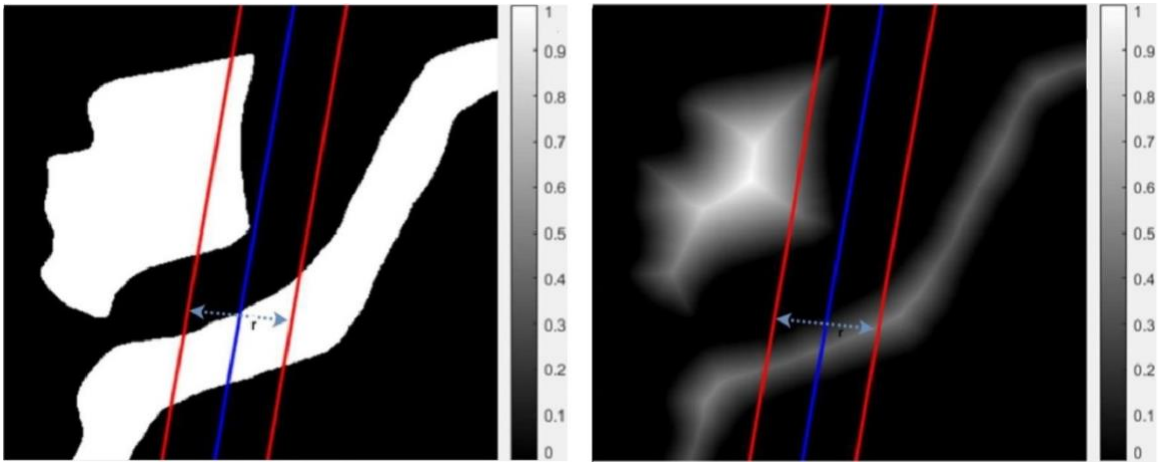


**Figure 11.** Calculation of the trajectory risk value. Blue: "Entry-Target" candidate trajectory, Red: ROI boundaries. Sparks et al. [29] approach (left), Proposed approach (right).

(Rota risk değerinin hesaplanması. Mavi: "Giriş-Hedef" aday rotası, Kırmızı: ROI sınırları. Sparks ve ark. [29] yaklaşımı (sol), Önerilen yaklaşım (sağ))

## 3. Results and Discussion (Sonuçlar ve Tartışma)

### 3.1. Analysis of Cerebral Vasculature (Beyin Damar Yapısının Analizi)

#### 3.1.1. Dataset (Veri kümesi)

The TubeTk dataset from the University of North Carolina was employed for brain vessel segmentation in this study. The dataset includes 100 pairs of MRI and MRA images acquired from healthy individuals using a Siemens Allegra 3T MR system [48], [49]. An important detail to note is that not all MRA images possess segmentation labels; only 42 images do. From these, 35 images formed the training set and 7 the test set. Data pre-processing encompassed converting segmentation labels into a format suitable for 3D segmentation via the 3D Slicer program, which is critical to enhancing the segmentation process's efficacy and accuracy.

#### 3.1.2. Implementation detail (Uygulama detayları)

The model was trained using the 3D Residual U-Net model and optimized with Dice Loss, a metric effective in segmentation problems. During the training, the Adam optimization algorithm was utilized, with 1e-4 set as the initial learning rate. The model was trained on NVIDIA's RTX A6000 GPU, with two samples at each training step, totaling 600 epochs. The process ensured successful training and testing of the model, enhancing its performance over time.

#### 3.1.3. Quantitative evaluation (Nicel değerlendirme)

In order to conduct a comprehensive quantitative evaluation of our model's performance, we leveraged a variety of widely accepted metrics to analyze the outputs from our test dataset [50]. These metrics included the Dice Similarity Coefficient (DSC) [51], Mean Absolute Error (MAE) [52], Hausdorff Distance (HD) [53], and the Structural Similarity Index (SSIM) [54]. By utilizing these different measures, we were able to provide a multi-faceted analysis that collectively offered a robust appraisal of the model's performance.

The Dice Similarity Coefficient (DSC), a common measure in segmentation tasks, evaluates the overlap between the model's predictions and the target. A high DSC value (0.8010) indicates that the model's segmentation results closely align with the target, suggesting a high level of accuracy. Mean Absolute Error (MAE), another metric, gauges the magnitude of errors made by the model. The low MAE value (0.0021) signals that the model's predictions are largely accurate, with a minimal deviation from the target values. Hausdorff Distance (HD), a more specific measure, calculates the greatest of all the distances from a point in one segmentation to the closest point in the other segmentation. Our model's HD value of 2.4614 shows that the model's segmentation results are generally quite close to the actual segmentation results. Lastly, the Structural Similarity Index (SSIM), measuring the structural similarity between two images, returned a high value of 0.9769 for our model. This suggests that the segmentation generated by the model effectively mimics the structural characteristics of the actual segmentation. Together, these metrics indicate a high overall segmentation performance of the model, generating results closely approximating the target segmentation results.

#### 3.1.4. Visual analysis (Görsel analiz)

Beyond numerical evaluation, we performed an in-depth visual analysis to further understand our model's performance in vascular segmentation in brain MRA images. We selected five different examples randomly from the test set and allowed our model to make predictions on these. For each image, we compiled a series of visuals featuring the input MRA image, the corresponding ground truth (actual segmentation), and the model-generated segmentation result. Due to the inherent complexity of representing 3D images on a 2D plane, we utilized the Maximum Intensity Projection (MIP) values of each image to streamline the visual comparison process. MIP, which projects 3D data onto a 2D plane, is particularly effective in visualizing the vascular network. These results, presented in a three-column format in Figure 12, provide a clear visual representation of the model's segmentation capabilities. The side-by-side display of the original MRA images, their actual segmentations (ground truth), and the MIPs of our model's segmentation results underscores the general similarity between the model's output and the actual segmentations, visually validating the model's robust segmentation performance.

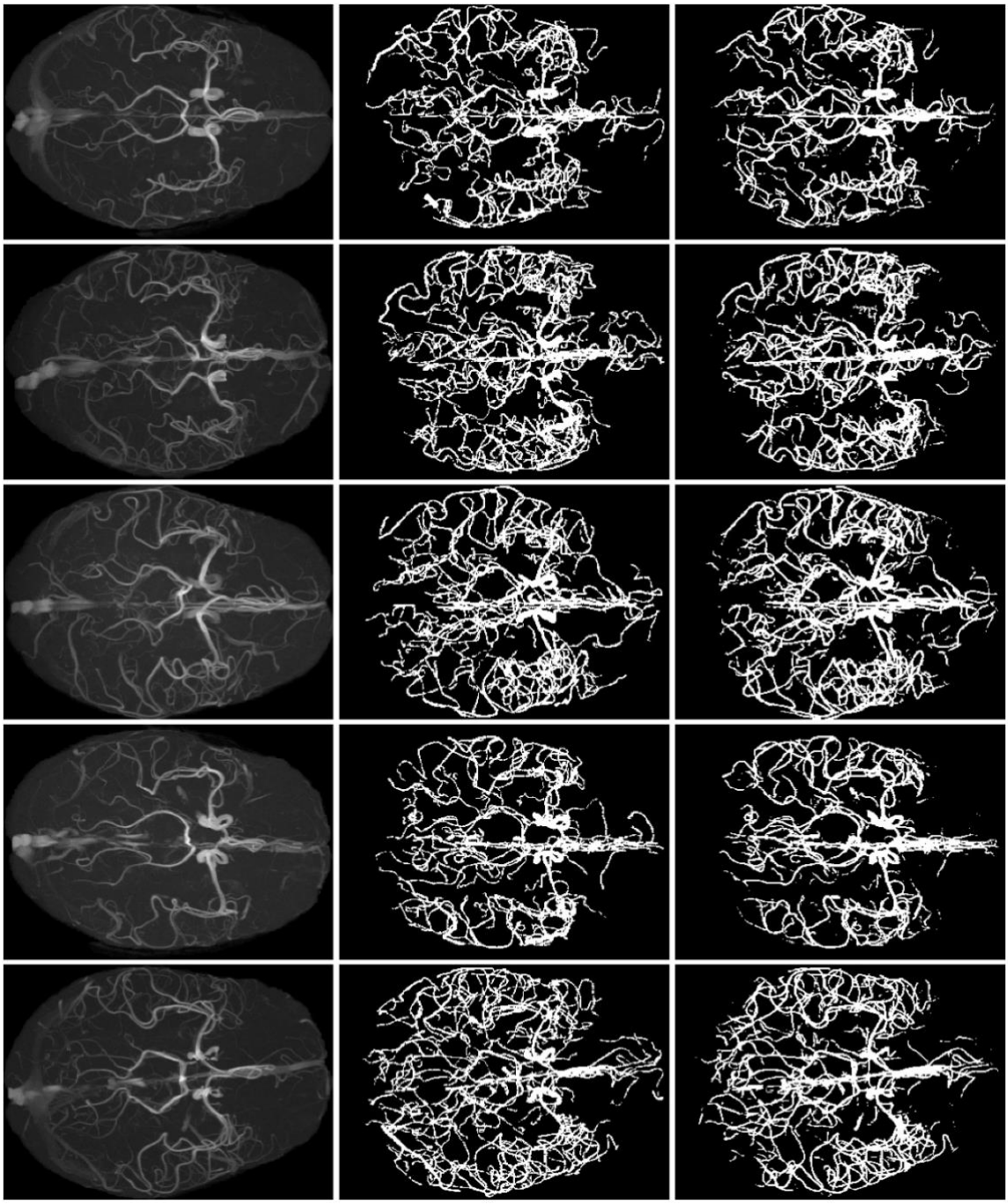

**Figure 12.** Side-by-side comparison of original MRA images, ground truth, and 3D Residual U-Net's segmentation results, visually validating the model's robust performance.

(Gerçek MRA görüntüleri, gerçek ve 3D Residual U-Net segmentasyon sonuçlarının yan yana karşılaştırması; modelin güçlü performansını görsel olarak doğrulamaktadır.)

### 3.2. Examination of Optimal Trajectory (En Uygun Rotanın İncelenmesi)

The 3D Slicer development environment has been preferred for the implementation activities of the proposed biopsy system. The fact that Slicer is open-source, free, and has an active community has been an important factor in this choice. Although it is written in C++, when a new module is to be added to Slicer, the Python programming language can be used. This feature allows Slicer to expand quickly. All sub-modules of the proposed biopsy system (Ventricle registration, Vascular tree segmentation, Entry point detection, etc.) are coded to run in Slicer software with Python programming language.

Figure 13 demonstrates visually how the optimal trajectory detection process is performed on an example patient MRI data using the developed software plugin. Firstly, the brain region (transparent

green area) is detected using MRI data. Then, the tumor structure (yellow structure inside) is manually segmented. After the segmentation process is completed, the center point of the tumor (target point) is calculated. Slicer's existing plugins are used for these operations. Next, surface points are obtained by performing model transformation of the brain region. Although the number of surface points is variable depending on the individual, it usually reaches the level of hundreds of thousands. Therefore, the point cloud is decimated to reduce this number to the level of hundreds. Then, the distances between each point in the point cloud and the target point are calculated, and the point (center point) with the shortest length is detected. Surface points within the circle centered on this point (candidate entries) are determined. After determining the candidate entries, the risk values of each candidate Entry-Target trajectory are calculated. The prism shown in Figure 10 is used for this purpose. Risk scores are calculated by evaluating vascular structures and functional structures within the prism. The risk scores calculated for 21 different trajectories are listed in Table 1. The results show that there is a strong relationship between the distance to the target and the risk score of the trajectory. When the results are carefully examined, it is observed that the trajectory with a shorter length does not necessarily have a lower risk score. However, in general, a proportional relationship was observed between the distance of the candidate entry point to the target and the trajectory risk value.

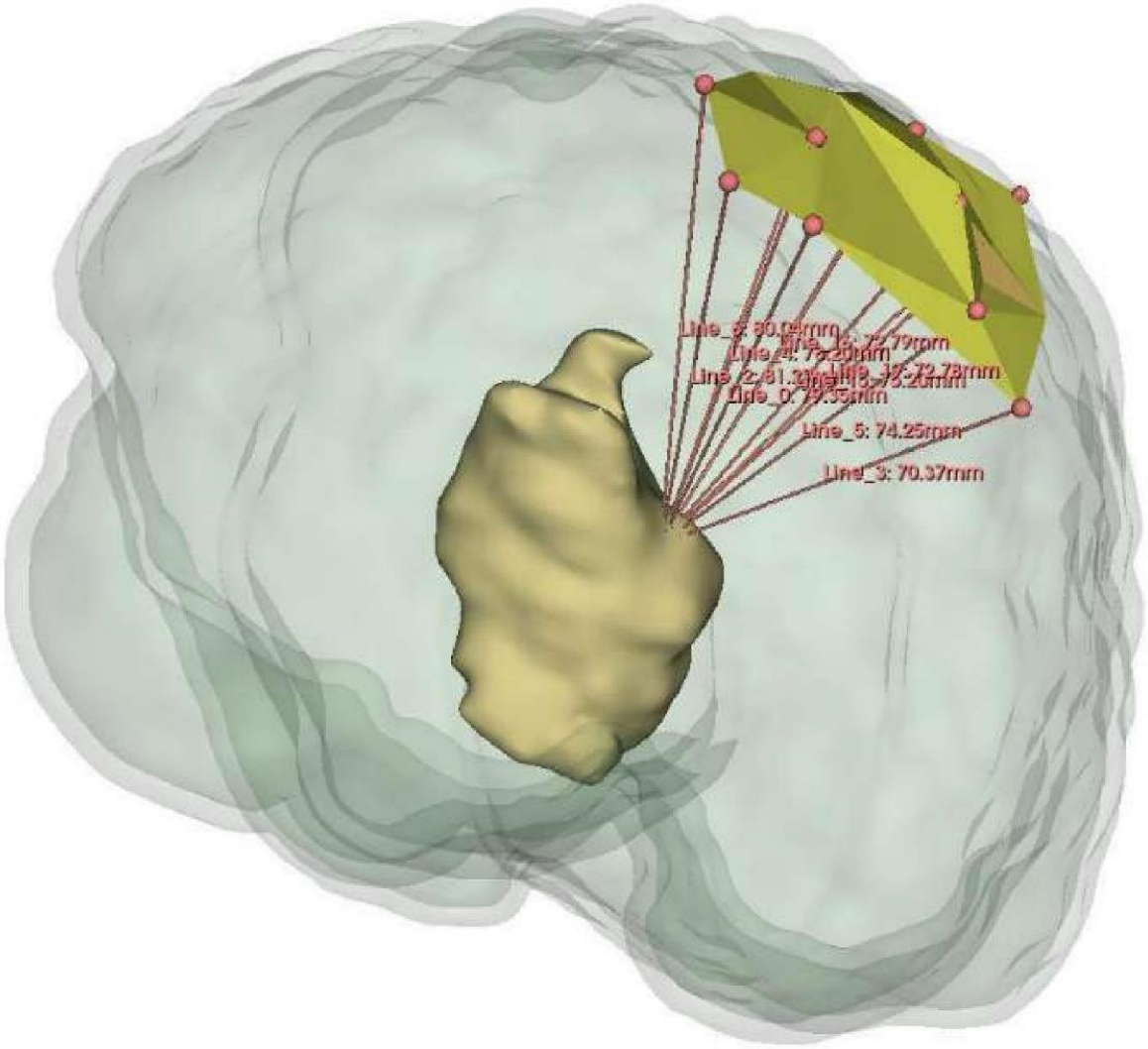


**Figure 13**. Visualization of the risk calculation process for candidate trajectories.

(Aday rotalara ilişkin risk hesaplama sürecinin görselleştirilmesi)

**Table 1**. Trajectories Distances and Risk Values. (Rotaların Mesafeleri ve Risk Değerleri.)

| Trajectories (Entry - Target) | Distance to Target (mm) | Risk Scores |
|---|---|---|
| $Candidate_{21}$ | 65.70 | 8698.48 |
| $Candidate_{19}$ | 72.78 | 9479.92 |
| $Candidate_{7}$ | 72.17 | 9729.64 |
| $Candidate_{3}$ | 70.37 | 9946.39 |
| $Candidate_{14}$ | 68.94 | 9965.16 |
| $Candidate_{20}$ | 69.93 | 10018.44 |
| $Candidate_{10}$ | 70.82 | 10372.35 |
| $Candidate_{18}$ | 71.63 | 10632.26 |
| $Candidate_{16}$ | 72.79 | 10749.02 |
| $Candidate_{17}$ | 70.57 | 10996.37 |
| $Candidate_{5}$ | 74.25 | 11070.54 |
| $Candidate_{15}$ | 75.20 | 11650.78 |
| $Candidate_{8}$ | 76.74 | 11675.82 |
| $Candidate_{13}$ | 73.29 | 11688.69 |
| $Candidate_{1}$ | 74.04 | 11837.02 |
| $Candidate_{12}$ | 78.30 | 12524.36 |
| $Candidate_{11}$ | 75.98 | 12525.06 |
| $Candidate_{0}$ | 79.35 | 12830.67 |
| $Candidate_{9}$ | 75.16 | 12902.58 |
| $Candidate_{4}$ | 78.20 | 13146.42 |
| $Candidate_{6}$ | 80.04 | 13902.70 |

### 3.3. Disadvantages of Classic Biopsy (Klasik Biyopsinin Dezavantajları)

There are some disadvantages of classic stereotactic biopsy. Firstly, it is performed in two sessions. Thus, the metal device is attached to the patient's head twice and imaging procedures are repeated twice. This leads to time and labor loss for both the patient and healthcare personnel. Additionally, there is a risk of damage or even fracture to the patient's skull during the attachment of the metal device. Secondly, manual marking and measurements on MRI images are performed by surgeons during the planning phase. This makes the success of the operation highly dependent on the surgeon's experience. The third disadvantage is the use of expensive biopsy software (such as Inomed, Brainlab, and Monteris) [55].

## 4. Conclusion (Sonuç)

This study presents a novel stereotactic brain biopsy system that utilizes MRI and MRA data from patients and incorporates automatic trajectory planning software to identify target and entry points. The distinguishing features of the proposed trajectory determination approach include: (1) the capability to perform the biopsy procedure in a single session, (2) full automation, (3) the first-time incorporation of skull thickness information in trajectory calculations, and (4) a unique trajectory risk score calculation method. The innovative trajectory risk score approach combines two risk values (geometric and structural). Geometric risk is assessed based on trajectory length, skull bone thickness, and alignment with the tumor's primary axis, while structural risk pertains to the trajectory's proximity to independent brain structures. Consequently, separate segmentation processes for brain structures (vascular network, ventricles, and functional areas) are conducted.

Moreover, an original method for calculating structural risk is employed. This technique converts segmented brain structures into gray scales (by assigning edge distances to structure voxels) and computes the risk by enclosing them within a rectangular prism. Current studies utilize fMRI (long-term, costly, and not widespread) to identify functional regions (motor, speech, vision, perception). In contrast, this study overlays a ready-made ATLAS dataset, with functional regions pre-determined by

surgeons using ventricular structures, onto the patient's MRI data. This allows for rapid detection of functional regions in patient data. Following the implementation of the proposed brain biopsy system, a proportional relationship was observed between the candidate entry point's distance to the target and the trajectory risk value. Future research plans encompass the development of novel methods for the detection of vasculature, tumor, and ventricles, as well as focusing on the refinement of the system's fully modular design.

## Acknowledgment (Teşekkür)

This study was supported by Scientific and Technological Research Council of Türkiye (TUBITAK) under the Grant Number 122E495. The authors thank to TUBITAK for their support.

## Conflict of Interest Statement (Çıkar Çatışması Beyanı)

No conflict of interest was declared by the authors.

## References (Kaynaklar)

[1] J. F. Arinez, Q. Chang, R. X. Gao, C. Xu, and J. Zhang, "Artificial intelligence in advanced manufacturing: Current status and future outlook," *J Manuf Sci Eng*, vol. 142, no. 11, p. 110804, 2020.

[2] S. Dörterler, S. Arslan, and D. Özdemir, "Unlocking the potential: A review of artificial intelligence applications in wind energy," *Expert Syst*, vol. 41, no. 12, p. e13716, 2024.

[3] E. Şahin and M. F. Talu, "Denim Kumaşından Otomatik Yüksek Çözünürlüklü Bıyık Desen Sentezi," *Computer Science*, pp. 86–100.

[4] S. Cakir, S. Toklu, and N. Yalcin, "RPL attack detection and prevention in the Internet of Things networks using a GRU based deep learning," *IEEE Access*, vol. 8, pp. 183678–183689, 2020.

[5] N. N. Arslan, E. Şahin, and M. Akçay, "Deep learning-based isolated sign language recognition: a novel approach to tackling communication barriers for individuals with hearing impairments," *Journal of Scientific Reports-A*, no. 055, pp. 50–59, 2023.

[6] J. P. Bharadiya, "Artificial intelligence in transportation systems a critical review," *American Journal of Computing and Engineering*, vol. 6, no. 1, pp. 35–45, 2023.

[7] H. Canli and S. Toklu, "Deep learning-based mobile application design for smart parking," *IEEE Access*, vol. 9, pp. 61171–61183, 2021.

[8] J. P. Bharadiya, "A comparative study of business intelligence and artificial intelligence with big data analytics," *American Journal of Artificial Intelligence*, vol. 7, no. 1, pp. 24–30, 2023.

[9] Y. Chang *et al.*, "A survey on evaluation of large language models," *ACM Trans Intell Syst Technol*, vol. 15, no. 3, pp. 1–45, 2024.

[10] M. A. Dursun and S. Serttaş, "A Multi-Metric Model for analyzing and comparing extractive text summarization approaches and algorithms on scientific papers," *Dicle Üniversitesi Mühendislik Fakültesi Mühendislik Dergisi*, vol. 15, no. 1, pp. 31–48, 2024.

[11] M. Şahin, E. Şahin, E. Özdemir, F. Talu, and S. Öztürk, "Beyin tümörü biyopsisi için derin öğrenme tabanlı risk minimizasyonlu otomatik planlama," *Gazi Üniversitesi Mühendislik Mimarlık Fakültesi Dergisi*, vol. 40, no. 1, pp. 487–500, 2025.

[12] S. A. Güven and M. F. Talu, "Brain MRI high resolution image creation and segmentation with the new GAN method," *Biomed Signal Process Control*, vol. 80, p. 104246, 2023.

[13] T. Davenport and R. Kalakota, "The potential for artificial intelligence in healthcare," *Future Healthc J*, vol. 6, no. 2, pp. 94–98, 2019.

[14] Ç. ERÇElİK and K. Hanbay, "Effects of Some Deep Learning Models with Power Law Transformation on Brain Tumor Classification," in *2024 8th International Artificial Intelligence and Data Processing Symposium (IDAP)*, IEEE, 2024, pp. 1–7.

[15] Ş. Karcı, "Farklı Otokodlayıcı Modelleri ile Sentetik Beyin MR Görüntülerinin Çoğaltılması," *Muş Alparslan Üniversitesi Mühendislik Mimarlık Fakültesi Dergisi*, vol. 2, no. 1, pp. 29–34, 2021.

[16] A. Al Kuwaiti *et al.*, "A review of the role of artificial intelligence in healthcare," *J Pers Med*, vol. 13, no. 6, p. 951, 2023.

[17] S. Das, G. K. Nayak, L. Saba, M. Kalra, J. S. Suri, and S. Saxena, "An artificial intelligence framework and its bias for brain tumor segmentation: A narrative review," *Comput Biol Med*, vol. 143, p. 105273, 2022.

[18] M. Trope *et al.*, "The role of automatic computer-aided surgical trajectory planning in improving the expected safety of stereotactic neurosurgery," *Int J Comput Assist Radiol Surg*, vol. 10, pp. 1127–1140, 2015.

[19] V. N. Vakharia *et al.*, "Computer-assisted planning for stereoelectroencephalography (SEEG)," *Neurotherapeutics*, vol. 16, no. 4, pp. 1183–1197, 2019.

[20] S. Khalighi, K. Reddy, A. Midya, K. B. Pandav, A. Madabhushi, and M. Abedalthagafi, "Artificial intelligence in neuro-oncology: advances and challenges in brain tumor diagnosis, prognosis, and precision treatment," *NPJ Precis Oncol*, vol. 8, no. 1, p. 80, 2024.

[21] R. Lynagh *et al.*, "Fluorescence-guided stereotactic biopsy: a proof-of-concept study," *J Neurosurg*, vol. 132, no. 2, pp. 530–536, 2019.

[22] I. Jung *et al.*, "Stereotactic biopsy for adult brainstem lesions: A surgical approach and its diagnostic value according to the 2016 World Health Organization Classification," *Cancer Med*, vol. 10, no. 21, pp. 7514–7524, 2021.

[23] A. Jaradat, A. Nowacki, J. Fichtner, J.-A. Schlaeppi, and C. Pollo, "Stereotactic biopsies of brainstem lesions: which approach?," *Acta Neurochir (Wien)*, vol. 163, pp. 1957–1964, 2021.

[24] G. Cheng *et al.*, "Complications of stereotactic biopsy of lesions in the sellar region, pineal gland, and brainstem: A retrospective, single-center study," *Medicine*, vol. 99, no. 8, p. e18572, 2020.

[25] N. Haj-Hosseini, J. C. O. Richter, P. Milos, M. Hallbeck, and K. Wårdell, "5-ALA fluorescence and laser Doppler flowmetry for guidance in a stereotactic brain tumor biopsy," *Biomed Opt Express*, vol. 9, no. 5, pp. 2284–2296, 2018.

[26] T. Ogiwara *et al.*, "A preliminary study of the diagnostic efficacy and safety of the novel boring biopsy for brain lesions," *Sci Rep*, vol. 12, no. 1, p. 4387, 2022.

[27] M. Zanello *et al.*, "Automated neurosurgical stereotactic planning for intraoperative use: a comprehensive review of the literature and perspectives," *Neurosurg Rev*, vol. 44, pp. 867–888, 2021.

[28] A. Higueras-Esteban *et al.*, "Projection-Based Collision Detection Algorithm for Stereoelectroencephalography Electrode Risk Assessment and Re-Planning," *IEEE Access*, vol. 9, pp. 105180–105191, 2021.

[29] H. J. Marcus, V. N. Vakharia, R. Sparks, R. Rodionov, N. Kitchen, and A. W. McEvoy, "Computer-Assisted Versus Manual Planning for Stereotactic Brain Biopsy: A Retrospective Comparative Pilot Study. Oper Neurosurg (Hagerstown). 2019 Aug 5," 2019.

[30] A. Kurmukov *et al.*, "Optimizing connectivity-driven brain parcellation using ensemble clustering," *Brain Connect*, vol. 10, no. 4, pp. 183–194, 2020.

[31] Y. Hu *et al.*, "A comparation between frame-based and robot-assisted in stereotactic biopsy," *Front Neurol*, vol. 13, p. 928070, 2022.

[32] Inomed, "inomed software," Inomed webpage. Accessed: Dec. 25, 2024. [Online]. Available: https://www.en.inomed.com/products/functional-neurosurgery/stereotactic-systems/

[33] A. Hatamizadeh, V. Nath, Y. Tang, D. Yang, H. R. Roth, and D. Xu, "Swin unetr: Swin transformers for semantic segmentation of brain tumors in mri images," in *International MICCAI brainlesion workshop*, Springer, 2021, pp. 272–284.

[34] Y. Tang *et al.*, "Self-supervised pre-training of swin transformers for 3d medical image analysis," in *Proceedings of the IEEE/CVF conference on computer vision and pattern recognition*, 2022, pp. 20730–20740.

[35] U. Baid *et al.*, "The rsna-asnr-miccai brats 2021 benchmark on brain tumor segmentation and radiogenomic classification," *arXiv preprint arXiv:2107.02314*, 2021.

[36] Project-MONAI, "SwinUNETR Code," Github. [Online]. Available: https://github.com/Project-MONAI/research-contributions/tree/main/SwinUNETR/BRATS21

[37] M. F. Talu, "Skull thickness map," 2022. [Online]. Available: https://github.com/fatihtalu/Slicer-ThicknessMap

[38] Y. Hua, Z. Yan, Z. Kuang, H. Zhang, X. Deng, and L. Yu, "Symmetry-aware deep learning for cerebral ventricle segmentation with intra-ventricular hemorrhage," *IEEE J Biomed Health*

*Inform*, vol. 26, no. 10, pp. 5165–5176, 2022.

[39] F. Ye, Z. Wang, S. Zhu, X. Li, and K. Hu, "A novel convolutional neural network based on adaptive multi-scale aggregation and boundary-aware for lateral ventricle segmentation on MR images," in *ICASSP 2022-2022 IEEE International Conference on Acoustics, Speech and Signal Processing (ICASSP)*, IEEE, 2022, pp. 1431–1435.

[40] J. B. Ginart *et al.*, "Multi-Modal Brain and Ventricle Segmentation Using Weakly Supervised Transfer Learning," 2021.

[41] B. Billot, C. Magdamo, Y. Cheng, S. E. Arnold, S. Das, and J. E. Iglesias, "Robust machine learning segmentation for large-scale analysis of heterogeneous clinical brain MRI datasets," *Proceedings of the National Academy of Sciences*, vol. 120, no. 9, p. e2216399120, 2023.

[42] A. Hilbert *et al.*, "BRAVE-NET: fully automated arterial brain vessel segmentation in patients with cerebrovascular disease," *Front Artif Intell*, vol. 3, p. 552258, 2020.

[43] G. Tetteh *et al.*, "Deepvesselnet: Vessel segmentation, centerline prediction, and bifurcation detection in 3-d angiographic volumes," *Front Neurosci*, vol. 14, p. 592352, 2020.

[44] E. Kerfoot, J. Clough, I. Oksuz, J. Lee, A. P. King, and J. A. Schnabel, "Left-ventricle quantification using residual U-Net," in *Statistical Atlases and Computational Models of the Heart. Atrial Segmentation and LV Quantification Challenges: 9th International Workshop, STACOM 2018, Held in Conjunction with MICCAI 2018, Granada, Spain, September 16, 2018, Revised Selected Papers 9*, Springer, 2019, pp. 371–380.

[45] O. Ronneberger, P. Fischer, and T. Brox, "U-net: Convolutional networks for biomedical image segmentation," in *Medical image computing and computer-assisted intervention–MICCAI 2015: 18th international conference, Munich, Germany, October 5-9, 2015, proceedings, part III 18*, Springer, 2015, pp. 234–241.

[46] NITRC, "Human brain atlas," Webpage. Accessed: Dec. 03, 2024. [Online]. Available: https://www.nitrc.org/projects/unc_brain_atlas/

[47] R. Sparks *et al.*, "Anatomy-driven multiple trajectory planning (ADMTP) of intracranial electrodes for epilepsy surgery," *Int J Comput Assist Radiol Surg*, vol. 12, pp. 1245–1255, 2017.

[48] KitwarePublic, " Tubetk Dataset," Webpage. Accessed: Oct. 22, 2024. [Online]. Available: https://public.kitware.com/Wiki/TubeTK/Data

[49] S. R. Aylward and E. Bullitt, "Initialization, noise, singularities, and scale in height ridge traversal for tubular object centerline extraction," *IEEE Trans Med Imaging*, vol. 21, no. 2, pp. 61–75, 2002.

[50] S. A. Güven, E. Şahin, and M. F. Talu, "Image-to-Image Translation with CNN Based Perceptual Similarity Metrics," *Computer Science*, vol. 9, no. 1, pp. 84–98, 2024.

[51] T. Sorensen, "A method of establishing groups of equal amplitude in plant sociology based on similarity of species content and its application to analyses of the vegetation on Danish commons," *Biologiske skrifter*, vol. 5, pp. 1–34, 1948.

[52] C. J. Willmott and K. Matsuura, "Advantages of the mean absolute error (MAE) over the root mean square error (RMSE) in assessing average model performance," *Clim Res*, vol. 30, no. 1, pp. 79–82, 2005.

[53] H. Federer, "Curvature measures," *Trans Am Math Soc*, vol. 93, no. 3, pp. 418–491, 1959.

[54] Z. Wang, A. C. Bovik, H. R. Sheikh, and E. P. Simoncelli, "Image quality assessment: from error visibility to structural similarity," *IEEE transactions on image processing*, vol. 13, no. 4, pp. 600–612, 2004.

[55] Medical Expo, "Neurosurgery softwares," Webpage. Accessed: Jan. 12, 2025. [Online]. Available: https://www.medicalexpo.com/medical-manufacturer/neurosurgery-software-16433.html